PNAS
www.pnas.org

# Supplementary Information for

## Guided transition waves in multistable metamaterials

**Lishuai Jin*, Romik Khajehtourian*, Jochen Mueller*, Ahmad Rafsanjani*, Vincent Tournat, Katia Bertoldi, Dennis M. Kochmann**

**Corresponding Authors: Katia Bertoldi and Dennis M. Kochmann**
**E-mail: bertoldi@seas.harvard.edu, dmk@ethz.ch**
***L.J., R.K., J.M., and A.R. contributed equally to this work and are listed in alphabetical order.**

### This PDF file includes:



### Other supplementary materials for this manuscript include the following:

## Supporting Information Text

## 1. Material and Fabrication

The material used in all structures is a thermoplastic acetal homopolymer resin (DuPont™, Midland, MI, USA) with a sheet thicknesses of $h = 1/16$ in, Young's modulus $E = 2.306\ GPa$, and Poisson's ratio $\nu$=0.35 (Fig. S1). Structures are laser cut (Universal Laser System PLS6.150D) using the following settings: the laser power is set to maximum, the speed to 12% of the maximum, PPI to 1000, the $z$-movement is turned off, the laser direction set to 'both' and the flow to 'air'. As shown in Fig. S2, the laser cutting process results in cuts with widths varying from approximately $w_b = 100\ \mu$m on the bottom face to $w_t = 600\ \mu$m on the top face. Point defects are introduced into the structure by inserting the negative of an open unit cell, i.e. filling the gaps of the open unit cell with a structure fabricated from transparent, acrylic sheets of $h = 1/8$ in (McMaster-Carr, Elmhurst, IL, USA) to prevent the unit cell from collapsing into its low-energy equilibrium state.

## 2. Experiments

**A. Uniaxial Tension Tests.** Uniaxial tensile and compression tests (Figs. S4-S8) are performed on a universal testing machine (Universal Testing Machine 5969, Instron, Norwood, MA, USA) according to ASTM D638-10. We first test the mechanical properties of the material using dogbone specimens with a test speed of 10 mm/min (specimen type IV; see Fig. S1). The results of these tests are used as an input to calibrate both the finite element (FE) and continuum models. Tensile/compression tests of the different multistable structures are performed at the same speed. To allow for transverse movement, required when testing structures with two or more columns under uniaxial tension, the samples were mounted in a test rig containing horizontal slots and two roller bearings for each joint (Fig. 1).

**B. Microscopy.** The unit cell geometry and laser cutting quality shown in Fig. S2 is analyzed via light microscopy (Keyence VHX 6000, Osaka, Osaka Prefecture, Japan) using a VH-Z20R ultra-small, high-performance zoom lens with a zoom range of 20× to 200×. Vertical images are stacked and processed by the software to create a 3D profile of the hinges and cuts.

**C. Analysis of Planar Waves.** Planar wave experiments are conducted on a flat acrylic plate with a second transparent acrylic plate placed above the samples to avoid any out-of-plane motion during the tests. During these tests we record the motion of the structures using a high-speed camera (SONY RX100V) at a frame rate of 480 fps and extract their local deformation using an open-source digital image correlation (DIC) and tracking package (1). We place a black circular marker at the center of each unit cell to track their positions and use that data to quantify the deformation through the relative change in area (see Eq. (1) in the manuscript).

## 3. Modeling

The modeling consists of two parts. FEA are used to simulate individual unit cells and small tessellations thereof (to complement the above experiments) with the objective of extracting the effective stress-strain curve and the stored energy density $\psi$ as a function of deformation under periodic boundary conditions. Results of the FE models (i.e., the energy density $\psi$ for a specific unit cell design) are fed into a continuum model, which has been developed for the efficient description of the time-dependent behavior of multistable structures and to explore the design space. Both models are described in the following.

**A. Finite Element Simulations.** To extract the effective mechanical response of a single unit cell, FEA are conducted using the commercial software package ABAQUS 6.14/Standard (Dassault Systèmes, Vélizy-Villacoublay, France). The Delrin base material of all structures is described by an elastic-plastic constitutive model, whose parameters are calibrated by comparison to the uniaxial tensile test data (Fig. S1). Each structure is discretized using finite-strain quadratic plane-stress elements (CPS8R and CPS6) and loaded by strain-driven periodic boundary conditions for the extraction of the homogenized stress-strain response. Localized penetration of structural features is avoided by modeling frictionless contact through a penalty constraint enforcement method with nonlinear stiffness in the normal contact direction. To promote convergence when contact is present, a dynamic implicit solver is used with moderate dissipation to determine the quasistatic response. The effect of unit cell geometry on its mechanical response is assessed through parameter studies using the Python scripting interface of ABAQUS. A laser beam thickness of 0.2 mm, which affects the fabricated geometries, is accounted for in the simulations (Fig. S2).

**B. Continuum model.** Inspired by constitutive models for phase transformations in solids, we propose a continuum model to describe the effective mechanical behavior behind the transition waves in multistable networks, which operates efficiently at the continuum level (hence being applicable to large structures) while taking into account information about the structural architecture in a homogenized fashion.

Supported by experiments, we neglect the effects of friction (the ground is smooth and the structure is assumed to slide freely), and we assume that inertial effects are negligible compared to the dissipation in the system. The latter stems from the viscoelastic response of the base material and is indeed required to produce constant-speed transition waves (2) (in a nutshell, the energy release from the bistable potential upon each snapping event is consumed by the viscous dissipation associated with the base material's deformation in response to the snapping event).

To describe the mechanical response of a sample made of the multistable structural architecture, we take a variational approach and define a strain energy density $W$ which characterizes the effective constitutive behavior. For convenience, we adhere to linearized kinematics to describe the deformation by the symmetric infinitesimal strain tensor $\boldsymbol{\varepsilon}$, which can be decomposed into a purely volumetric contribution, $\theta = \mathrm{tr}(\boldsymbol{\epsilon})/d$, and a deviatoric (i.e., volume-preserving) contribution, $\boldsymbol{e} = \boldsymbol{\varepsilon} - \theta \boldsymbol{I}$. (The extension to finite strains is technically straight-forward, yet we expect no new physics so the linearized description is chosen here for illustrative simplicity.) Observing that the bistability of a unit cell is of volumetric nature (the two equilibrium states are characterized by the open and closed configurations, distinguished by a volumetric strain), we assume that the strain energy density is of the additive form

$$W(\boldsymbol{\varepsilon}) = \psi(\theta) + W_{\mathrm{dev}}(\boldsymbol{e}) = \psi(\theta) + \frac{\mu}{2} \|\boldsymbol{e}\|^2 , \qquad [1]$$

where

$$\psi(\theta) = c_0 + c_1\theta + c_2\theta^2 + c_3\theta^3 + c_4\theta^4 \qquad [2]$$

is an equation of state which is here linked to the non-convex potential energy density of a unit cell (calculated by FEA, see above, and fitted to a quartic polynomial for ease of analytical differentiation). $W_{\mathrm{dev}}(\boldsymbol{e}) = \frac{\mu}{2} \|\boldsymbol{e}\|^2$ represents an effective energy density penalizing changes in deformation between neighboring unit cells. This latter energy contribution vanishes within homogeneous domains (where all unit cells deform in the same volumetric fashion), so it only arises in and close to domain boundaries and hence stands for an effective interface energy density with a phenomenological

modulus $\mu > 0$. We acknowledge that the above energy density is, of course, not the only possible form to describe the transition front behavior. However, it accurately and efficiently captures the salient features observed in experiments and is therefore used here.

By following classical Coleman-Noll theory, the associated infinitesimal stress tensor, describing the bistable elastic response, follows as

$$\boldsymbol{\sigma}_{\mathrm{e}} = \frac{\partial W}{\partial \boldsymbol{\varepsilon}} = \frac{\psi'(\theta)}{d}\boldsymbol{I} + \mu \boldsymbol{e}. \qquad [3]$$

In addition to the above elastic contribution to the stress tensor, the viscoelastic nature of the base material causes viscous stresses that counter deformation in a time-dependent fashion. As a leading-order approximation, we here assume linear viscosity and introduce a viscous stresses tensor contribution $\boldsymbol{\sigma}_{\mathrm{v}} = \eta \dot{\boldsymbol{\varepsilon}}$ with a Newtonian viscosity parameter $\eta \geq 0$ (non-negative by the second law of thermodynamics), and dots denoting time derivatives. Overall, the stress tensor thus becomes

$$\boldsymbol{\sigma} = \boldsymbol{\sigma}_{\mathrm{e}} + \boldsymbol{\sigma}_{\mathrm{v}} = \frac{\psi'(\theta)}{d}\boldsymbol{I} + \mu \boldsymbol{e} + \eta \dot{\boldsymbol{\varepsilon}}. \qquad [4]$$

The time-dependent deformation of the body on the macroscale is governed by the conservation of linear momentum (in the absence of body forces and with negligible inertia), which requires

$$\operatorname{div} \boldsymbol{\sigma} = \boldsymbol{0} \qquad \Leftrightarrow \qquad \operatorname{div}\left(\frac{\psi'(\theta)}{d}\boldsymbol{I} + \mu \boldsymbol{e} + \eta \dot{\boldsymbol{\varepsilon}}\right) = \boldsymbol{0}. \qquad [5]$$

By assuming that $\mu$ and $\eta$ are constant material parameters, the above is equivalent to

$$\frac{1}{d}\left(\frac{\psi''(\theta)}{d} - \mu\right) \operatorname{grad}(\operatorname{tr} \boldsymbol{\varepsilon}) + \mu \operatorname{div} \boldsymbol{\varepsilon} + \eta \operatorname{div} \dot{\boldsymbol{\varepsilon}} = \boldsymbol{0}. \qquad [6]$$

Invoking the strain–displacement relation $\boldsymbol{\varepsilon} = \operatorname{sym}(\nabla \boldsymbol{u})$ with the displacement field $\boldsymbol{u} : \Omega \to \mathbb{R}^d$ defined across a macroscopic body $\Omega$, we transform Eq. (6) into

$$\frac{\eta}{2}(\dot{u}_{i,kk} + \dot{u}_{k,ki}) + \left(\frac{\psi''(u_{k,k}/d)}{d^2} - \frac{\mu}{d}\right) u_{k,ki} + \frac{\mu}{2}(u_{i,kk} + u_{k,ki}) = 0, \qquad [7]$$

where we used index notation with Einstein's summation convention and subscripts following a comma denoting partial derivatives with respect to spatial coordinates.

The system of partial differential equations Eq. (7) is solved with given boundary conditions, using an in-house finite element code which discretizes the 2D bodies of interest by a regular mesh of linear triangular (CST) elements and uses a backward-Euler scheme for implicit time integration with a time step size $\Delta t$ (using a Newton-Raphson iterative solver).

The link between this continuum description of a sample and the characteristics of the underlying unit cell is established explicitly through the interaction potential $\psi$ (defining the interaction energy in any link between unit cells) and implicitly through modulus $\mu$ and viscosity $\eta$. The latter two parameters are introduced as an efficient means to capture the large-scale behavior. We turn to homogenization theory to link those model parameters to the unit cell specifics (the procedure can generally be applied to other unit cells and is not limited to the specific design employed here). Following first-order homogenization, we assume that any macroscale deformation state, characterized by a strain tensor $\boldsymbol{\varepsilon}$, results in an affine deformation of the microscale unit cell deforming by the same homogeneous strains $\boldsymbol{\varepsilon}$ (rigid-body motion being irrelevant here due to negligible inertia). Since

unit cells are arranged in a triangular lattice, which is generally characterized by stiff, stretching-dominated behavior, the affine deformation assumption – though generally providing only an upper bound – is a realistic leading-order approximation.

We consider a unit cell $\Omega$ with volume $V$, which is connected to its six neighboring unit cells. Without loss of generality, we choose the center of the unit cell at $\boldsymbol{x}_0 = \boldsymbol{0}$ to be the origin of the local coordinate frame, so that the affine deformation of the unit cell (characterized by a volumetric expansion with volumetric strain $\theta$ and superimposed strains $\boldsymbol{\epsilon}$) imposes displacements $\boldsymbol{u}(\boldsymbol{x}) = (\theta\boldsymbol{I} + \boldsymbol{\epsilon})\boldsymbol{x} = \boldsymbol{\varepsilon}\boldsymbol{x}$. Consequently, the displacement of the center of the $\alpha$-th neighboring unit cell ($\alpha = 1, \dots, 6$), originally located at $\boldsymbol{x}_\alpha$, is $\boldsymbol{u}_\alpha = (\theta\boldsymbol{I} + \boldsymbol{\epsilon})\boldsymbol{x}_\alpha$. We further note that the undeformed distance vector from the origin to each neighboring unit cell center is $\boldsymbol{x}_\alpha - \boldsymbol{x}_0 = \boldsymbol{x}_\alpha$, while the corresponding deformed distance vector is given by

$$\boldsymbol{r}_\alpha = \boldsymbol{u}_\alpha + \boldsymbol{x}_\alpha - (\boldsymbol{x}_0 + \boldsymbol{u}_0) = \boldsymbol{u}_\alpha + \boldsymbol{x}_\alpha = [(\theta + 1)\boldsymbol{I} + \boldsymbol{\epsilon}]\boldsymbol{x}_\alpha = (\boldsymbol{\varepsilon} + \boldsymbol{I})\boldsymbol{x}_\alpha. \tag{8}$$

We define the effective energy density of a unit cell $\Omega$ undergoing strains $\boldsymbol{\varepsilon}$ as the average energy density

$$W_\Omega(\boldsymbol{\varepsilon}) = \frac{1}{2}\sum_{\alpha=1}^{6} \psi(\varepsilon_\alpha), \tag{9}$$

where $\psi$ represents the elastic interaction energy dependent on the 1D strains $\varepsilon_\alpha = (\|\boldsymbol{r}_\alpha\| - \|\boldsymbol{x}_\alpha\|)/\|\boldsymbol{x}_\alpha\|$ in each link between unit cell $\Omega$ and its six neighboring unit cells. Inserting the above macro-to-micro transition relations hence yields

$$\varepsilon_\alpha = \frac{\|\boldsymbol{r}_\alpha\| - \|\boldsymbol{x}_\alpha\|}{\|\boldsymbol{x}_\alpha\|} = \frac{\|\boldsymbol{r}_\alpha\|}{\|\boldsymbol{x}_\alpha\|} - 1 = \|(\boldsymbol{\varepsilon} + \boldsymbol{I})\hat{\boldsymbol{x}}_\alpha\| - 1 \tag{10}$$

where $\hat{\cdot} = (\cdot)/\|\cdot\|$ denotes a unit vector. We note that the factor $1/2$ in Eq. (9) corrects for double-counting of each interaction link when composing the total energy of the network.

Differentiating the effective energy density yields the effective elastic stress tensor and its components:

$$\boldsymbol{\sigma}_\mathrm{e} = \frac{\partial W_\Omega}{\partial \boldsymbol{\varepsilon}} \qquad \Rightarrow \qquad \sigma_{ij} = \frac{1}{2}\sum_{\alpha=1}^{6} \frac{\partial \psi}{\partial \varepsilon}(\varepsilon_\alpha)\frac{\partial \varepsilon_\alpha}{\partial \varepsilon_{ij}}, \tag{11}$$

and the incremental stiffness tensor of fourth order is derived analogously, having components

$$\mathbb{C} = \frac{\partial \boldsymbol{\sigma}_\mathrm{e}}{\partial \boldsymbol{\varepsilon}} \qquad \Rightarrow \qquad \mathbb{C}_{ijkl} = \frac{1}{2}\sum_{\alpha=1}^{6}\left[\psi''(\varepsilon_\alpha)\frac{\partial \varepsilon_\alpha}{\partial \varepsilon_{ij}}\frac{\partial \varepsilon_\alpha}{\partial \varepsilon_{kl}} + \psi'(\varepsilon_\alpha)\frac{\partial^2 \varepsilon_\alpha}{\partial \varepsilon_{ij}\,\partial \varepsilon_{kl}}\right]. \tag{12}$$

The derivatives in Eq. (11) and Eq. (12) can be expressed, using Eq. (10) and exploiting the symmetry of the strain tensor, as

$$\frac{\partial \varepsilon_\alpha}{\partial \varepsilon_{ij}} = \frac{1}{2}\left[(\hat{\boldsymbol{r}}_\alpha)_i(\hat{\boldsymbol{x}}_\alpha)_j + (\hat{\boldsymbol{x}}_\alpha)_i(\hat{\boldsymbol{r}}_\alpha)_j\right], \tag{13}$$

writing $(\boldsymbol{x})_i$ for the $i$-th component of vector $\boldsymbol{x}$. Analogously, we arrive at

$$\begin{aligned}\frac{\partial^2 \varepsilon_\alpha}{\partial \varepsilon_{ij}\,\partial \varepsilon_{kl}} = \frac{1}{2}\Big[&(\delta_{ik}(\hat{\boldsymbol{r}}_\alpha)_l(\hat{\boldsymbol{x}}_\alpha)_j + \delta_{jk}(\hat{\boldsymbol{x}}_\alpha)_i(\hat{\boldsymbol{r}}_\alpha)_l) \\ &- \frac{1}{2}\left((\hat{\boldsymbol{r}}_\alpha)_i(\hat{\boldsymbol{x}}_\alpha)_j + (\hat{\boldsymbol{x}}_\alpha)_i(\hat{\boldsymbol{r}}_\alpha)_j\right)\Big((\hat{\boldsymbol{r}}_\alpha)_k(\hat{\boldsymbol{r}}_\alpha)_l + (\hat{\boldsymbol{r}}_\alpha)_k(\hat{\boldsymbol{r}}_\alpha)_l\Big)\Big].\end{aligned} \tag{14}$$

In order to reconcile the empirical energy density formulated in Eq. (1) with the homogenized energy density Eq. (9) (and to reduce Eq. (9) to a simple analytical expression), we exploit that the volumetric deformation is essential in capturing the bistability, while deviatoric effects primarily affect domain boundary regions. To this end, we use the decomposition

$$\boldsymbol{\varepsilon} = \theta \boldsymbol{I} + \boldsymbol{\epsilon} \tag{15}$$

and expand the homogenized energy density $W_\Omega(\boldsymbol{\varepsilon}) \equiv W_\Omega(\theta, \boldsymbol{\epsilon})$ from Eq. (9) about $\boldsymbol{\varepsilon} = \theta \boldsymbol{I}$ up to quadratic order in $\boldsymbol{\epsilon}$:

$$\begin{aligned} W_\Omega &= W_\Omega(\theta, \mathbf{0}) + \frac{\partial W_\Omega}{\partial \varepsilon_{ij}}(\theta, \mathbf{0})\, \epsilon_{ij} + \frac{1}{2} \frac{\partial^2 W_\Omega}{\partial \varepsilon_{ij}\, \partial \varepsilon_{kl}}(\theta, \mathbf{0})\, \epsilon_{ij} \epsilon_{kl} + \text{h.o.t.} \\ &= W_\Omega(\theta, \mathbf{0}) + \sigma_{ij}(\theta, \mathbf{0}) \epsilon_{ij} + \frac{1}{2} \mathbb{C}_{ijkl}(\theta, \mathbf{0}) \epsilon_{ij} \epsilon_{kl} + \text{h.o.t.} \end{aligned} \tag{16}$$

Towards a numerically convenient simplification (which also admits a cleaner interpretation), we choose $\theta = \theta_0 = \text{const.}$ and hence evaluate the above expansion about the undeformed ground state. This leads to $\psi'(\theta_0) = 0$ and $\boldsymbol{x}_\alpha = \boldsymbol{r}_\alpha$, and hence

$$W_\Omega \approx W_\Omega(\theta_0, \mathbf{0}) + \frac{1}{4} \psi''(\theta_0) \sum_{\alpha=1}^{n} (\hat{\boldsymbol{x}}_\alpha)_i (\hat{\boldsymbol{x}}_\alpha)_j (\hat{\boldsymbol{x}}_\alpha)_k (\hat{\boldsymbol{x}}_\alpha)_l\, \epsilon_{ij} \epsilon_{kl} = \psi(\theta) + \frac{1}{2} \epsilon_{ij} \mathbb{C}^{\text{approx.}}_{ijkl} \epsilon_{kl} \tag{17}$$

with the approximated stiffness tensor

$$\mathbb{C}^{\text{approx.}}_{ijkl} = \frac{1}{2} \psi''(\theta_0) \sum_{\alpha=1}^{6} (\hat{\boldsymbol{x}}_\alpha)_i (\hat{\boldsymbol{x}}_\alpha)_j (\hat{\boldsymbol{x}}_\alpha)_k (\hat{\boldsymbol{x}}_\alpha)_l. \tag{18}$$

The obtained homogenized energy density Eq. (17) is analogous to the empirical energy density Eq. (1). (Of course, the resulting model will depend on the choice of $\theta_0$ in the above expansion; results show convincing agreement between experimental data and numerical predictions for this particular choice made here.)

For the 2D triangular lattice configuration chosen here, the components of the above contribution to the stiffness tensor evaluate to

$$\mathbb{C}^{\text{approx.}}_{ijkl} = \tilde{\lambda} \delta_{ij} \delta_{kl} + \tilde{\mu} (\delta_{ik} \delta_{jl} + \delta_{il} \delta_{jk}) \qquad \text{with} \qquad \tilde{\lambda} = \tilde{\mu} = \frac{3}{8} \psi''(\theta_0)\,. \tag{19}$$

This is the classical form of isotropic linear elasticity. The empirical continuum model introduced in Eq. (1) replaces $\tilde{\lambda}$ by the bistable equation of state for the volumetric contribution. The above shows that a reasonable choice for the empirical modulus $\mu$ introduced in Eq. (1) is given by $\mu = \frac{3}{8} \psi''(\theta_0)$.

Finally, the second model parameter, the viscosity $\eta$, depends on the properties of the polymeric base material and is harder to quantify. However, it directly governs the speed and kinetics of the domain evolution process, so that $\eta$ can be quantified by fitting to experimental data – which is the approach that was chosen for all simulations here. All model parameters used for simulations are summarized in Table S1.

Simulations using the continuum model were conducted using an in-house FE code; initial boundary value problems were solved by a Newton-Raphson solver. We used triangular (CST) elements for all 2D simulations and confirmed mesh convergence through $h$-refinement. Point defects were implemented through stiff bar elements (approximating rigid links). The tube simulation in Fig. 5c was performed by meshing a thin-walled hollow tube with tetrahedral (CST) solid elements in 3D and using the above empirical material model with $d = 3$.

| Figure number | constants of Eq. (2), i.e., $\{c_0, c_1, c_2, c_3, c_4\}$ | viscosity per time step, $\eta/\Delta t$ | empirical shear modulus $\mu$ |
|---|---|---|---|
| Figure 3 | $\{0, 0.0085, 0.641, -4.1456, 6.8689\} \times 10^6$ | $0.673 \times 10^6$ | $1.923 \times 10^6$ |
| Figure 4 | $\{0, 0.010, 0.705, -4.70, 7.89\} \times 10^6$ | $0.673 \times 10^6$ | $2.115 \times 10^6$ |
| Figure 5a | $\{0, 0.016, 0.6058, -4.6426, 8.6121\} \times 10^6$ | $1.810 \times 10^5$ | $1.210 \times 10^6$ |
| Figure 5b | $\{0, 0.127, 0.7556, -8.6, 17.082\} \times 10^6$ | $1.210 \times 10^6$ | $1.511 \times 10^6$ |
| Figure 5c (A) | $\{0, 0.124, 0.2054, -5.18, 11.443\} \times 10^6$ | $0.724 \times 10^6$ | $0.411 \times 10^6$ |
| Figure 5c (B) | $\{0, 0.127, 0.7556, -8.6, 17.082\} \times 10^6$ | $0.724 \times 10^6$ | $1.511 \times 10^6$ |
| Figure 5c (C) | $\{0, 0.016, 0.6058, -4.6426, 8.6121\} \times 10^6$ | $0.724 \times 10^6$ | $1.212 \times 10^6$ |
| Figure 5c (D) | $\{0, 0.0045, 1.0, -6.9, 12.36\} \times 10^6$ | $0.724 \times 10^6$ | $2.000 \times 10^6$ |

**Table S1. Values of all parameters used by the continuum model. We point out that, while Fig. 4 was generated using a constant set of parameters, results in Fig. 3 used a slightly modified parameter set, as indicated above, to account for the free-surface effects in the finite structure used in experiments. Parameters for Fig. 5c have been chosen, as shown above, to produce the reported variations in transition front speed.**

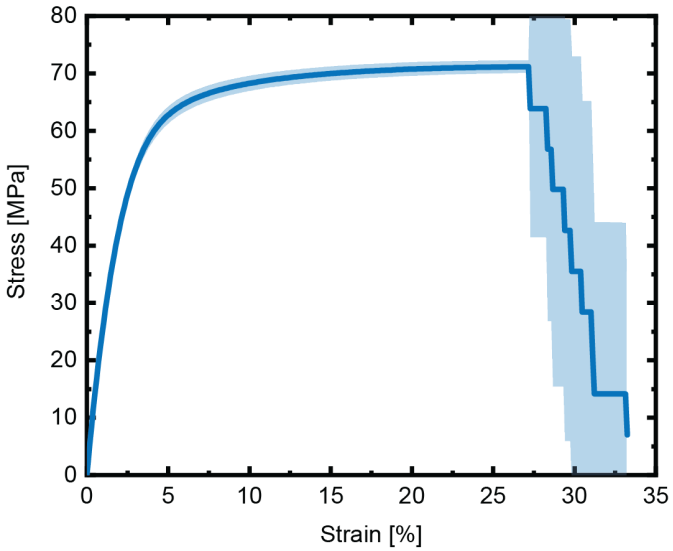


**Fig. S1.** Tensile test results from dogbone specimens (ASTM D638, type IV) tested on a universal testing machine. The curve shows the mean of the n=10 samples (solid line) and their standard deviation (shaded area). Note that all samples failed catastrophically; the stepwise failure of the mean curve is due to averaging over all samples.

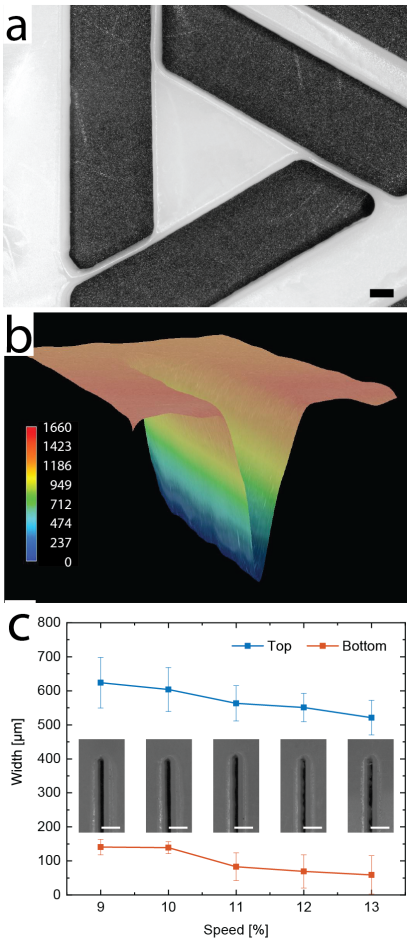


**Fig. S2.** Analysis of the cut geometry as fabricated by a laser cutter: (a) top view showing a unit cell's features, using a light microscope. (b) A 3D depth scan of the cut gap shows an increasing width from the bottom to the top. Note that the bottom of the gap starts at around 400 $\mu$ m. (c) Quantitative analysis of the 3D depth profiles from microscopy. Statistically averaged over five tested samples.

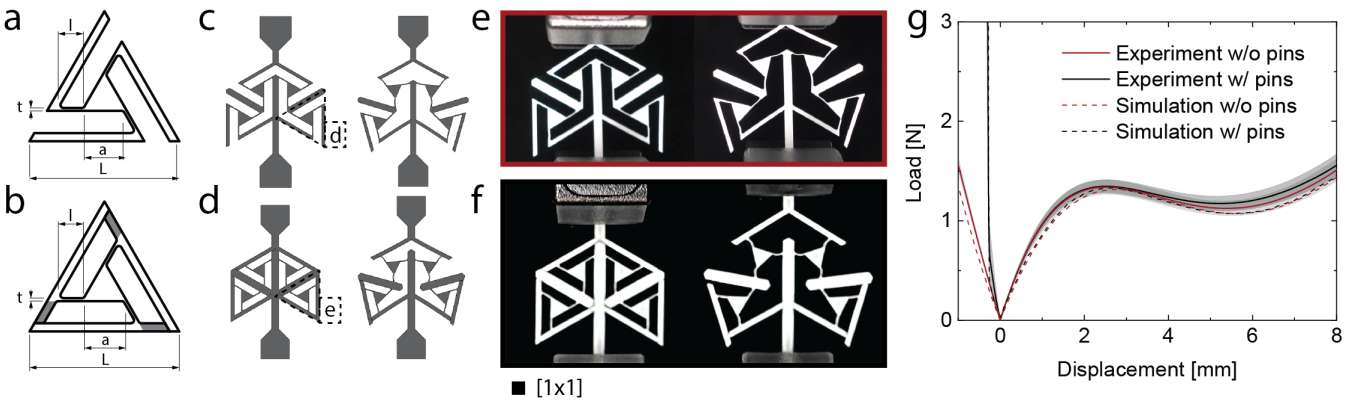


**Fig. S3.** Effect of pins on the mechanical properties of the unit cells: (a,b) unit cell features with and without pins; (c,d) both geometries are embedded in a dogbone specimen geometry and tested numerically in compression and tension; (e,f) experimental uniaxial tensile tests of the two specimen types show a qualitatively similar deformation behavior; (g) quantitative analysis shows a similar behavior in the tensile regime (positive displacement), but a noticeable difference in the compression regime (negative displacement), where the unit cell with pins is considerably stiffer. The shading illustrates the standard deviation calculated from 5 samples.


**Fig. S4.** Different unit cell tessellations tested in uniaxial tension. The combinations range from one row to three rows and from one column to three columns, covering the monostable and multistable regions as well as the transition region, shown in the phase map in Fig. S8.

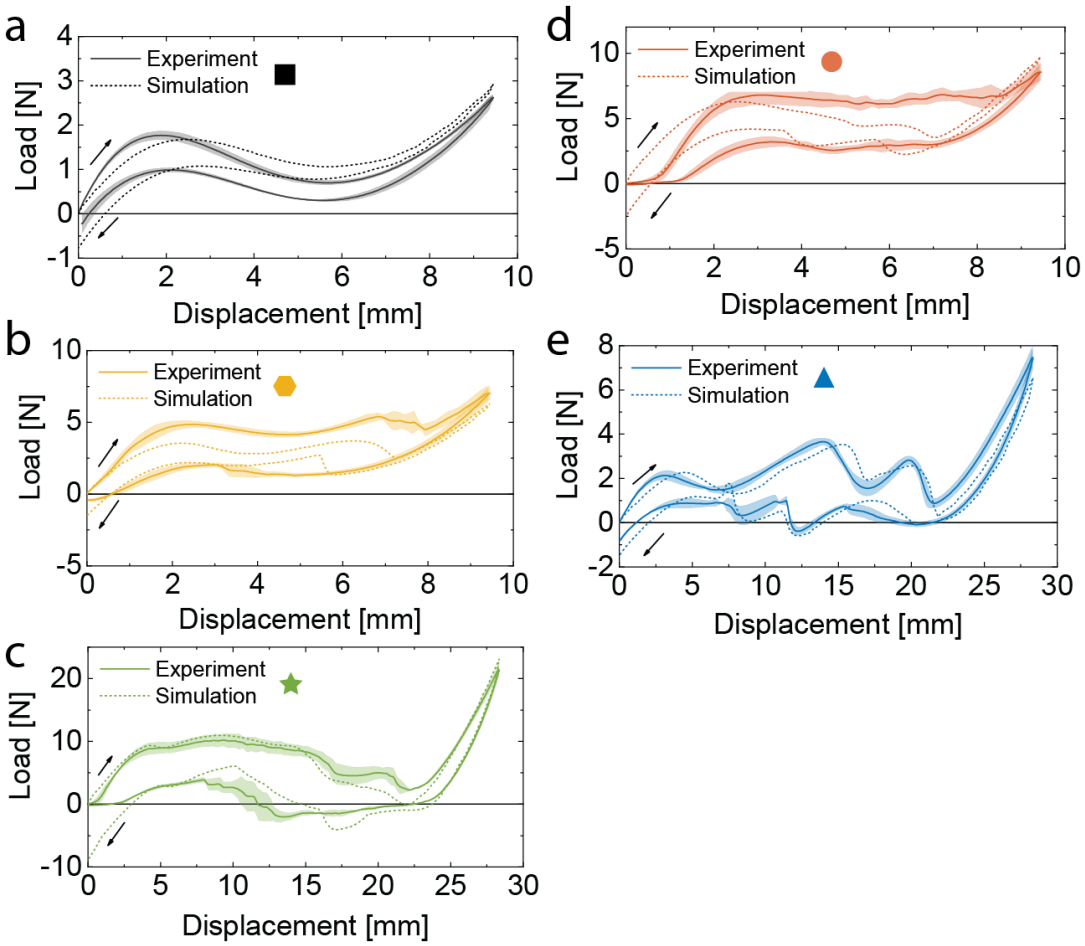


**Fig. S5.** Quantitative analysis of the uniaxial tensile tests shown in Fig. S4. The five cases refer to the tessellations in Fig. S4 (indicated by the symbols): (a) $1 \times 1$ unit cell, (b) $2 \times 1$ unit cell, (c) $3 \times 3$ unit cell, (d) $3 \times 1$ unit cell, and (e) $1 \times 3$ unit cell, where the first number refers to the number of (vertical) columns and the second number to the number of (horizontal) rows.

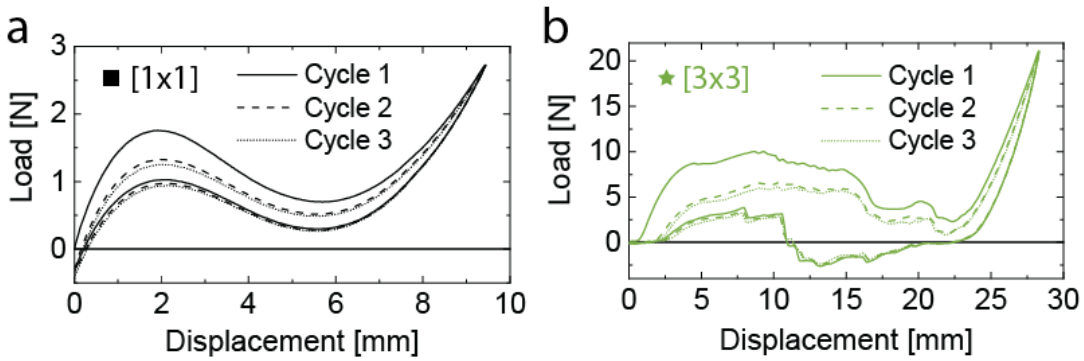


**Fig. S6.** Representative curves of three consecutive cycles from the experimental uniaxial tensile tests shown in Fig. S4. (a) $1 \times 1$ unit cell, (b) $3 \times 3$ unit cell. Some level of plastic deformation (localized near the hinges) is inevitable during the initial cycles, but the cyclic response stabilizes soon after the first cycle, as shown.

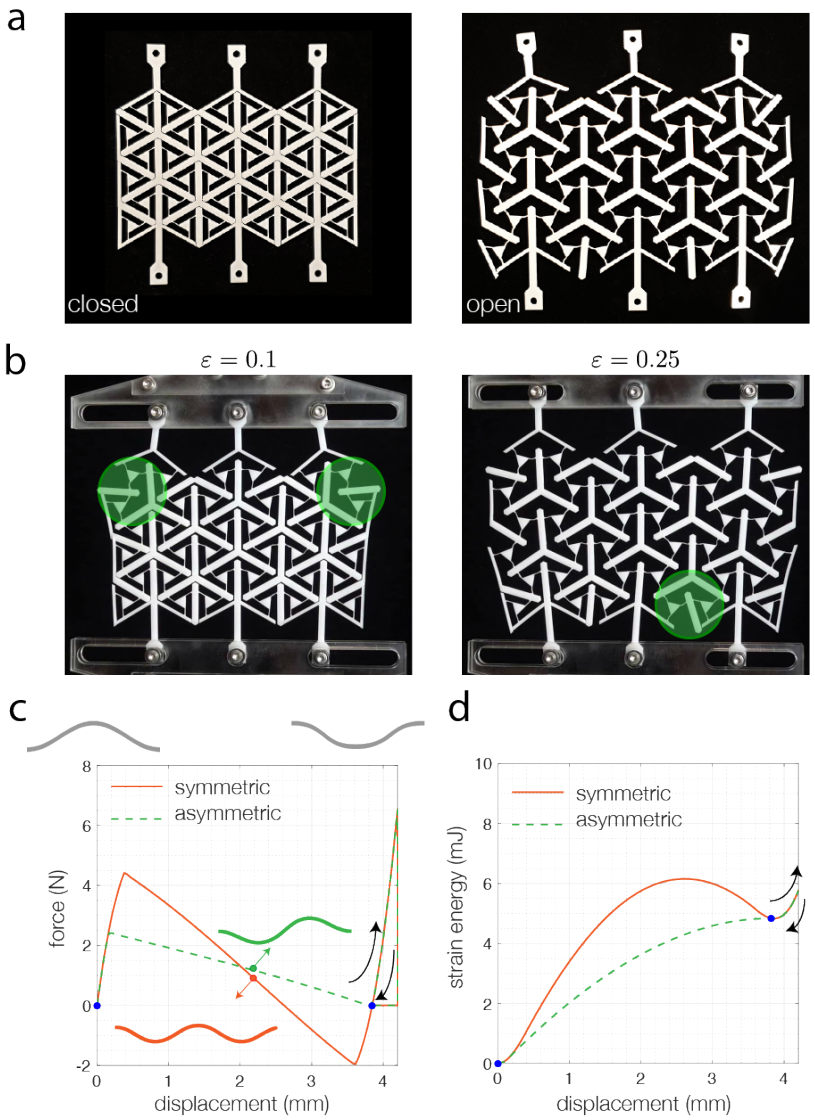


**Fig. S7.** (a) closed and open states of the $3 \times 3$ structure, both of which are stable (despite the load-displacement curve remaining above zero in our experiments - see Fig. S5-c). (b) This behavior can be attributed to asymmetric deformation modes triggered during loading. (c)-(d) To demonstrate this point, we focus on a simple elastic curved beam with profile described by $y = A/2[1 - \cos(2\pi x/L)]$ ($x \in [0,\ L]$) and square cross-section of edge $h$. Such a beam is known to be bistable when it is subjected to a mid-point displacement if $A/h > 2.31$ (3). We choose $L = 10$ mm, $A = 2$ mm and $h = 0.67$ mm (so that $A/h = 3 > 2.31$) and conduct finite elements with ABAQUS to capture its response. Specifically, we mesh the beam using 2D Timoshenko beam elements and use an isotropic linear elastic constitutive model to capture the response of the material (with Young's modulus $E = 3.85$ GPa and Poisson's ratio $\nu = 0.4$). We impose a vertical displacement, $u_z = 4.2$ mm, to its middle point and use an implicit dynamics solver to follow its deformation. Finally, we deactivate the imposed displacement and verify that the deformed configuration is stable by examining if the structure maintains its deformed shape. In our first simulation we constrain the horizontal displacement of the central point as we apply $u_z$. In this case the beam follows a symmetric deformation path and, as expected, the measured force is characterized by a negative region (see red line in (c)) and the strain energy shows two clear local minima (see red line in (d)). By contrast, when we remove the horizontal constraint at the central point, the beam follows an asymmetric deformation path to reach the final configuration (see green insert in (c)). In this case the measured force is always positive (see the green line in (c)) and approaches zero only at a specific point. Moroever, the strain energy at that point shows an extremum without a distinct energy barrier (see green line in (d)). However, the beam remains in the deformed configuration when the force is removed – a clear indication of bistability. As such, this simple example demonstrates that an asymmetric deformation mode can bring a structure to another stable configuration without reversing the sign of the force.

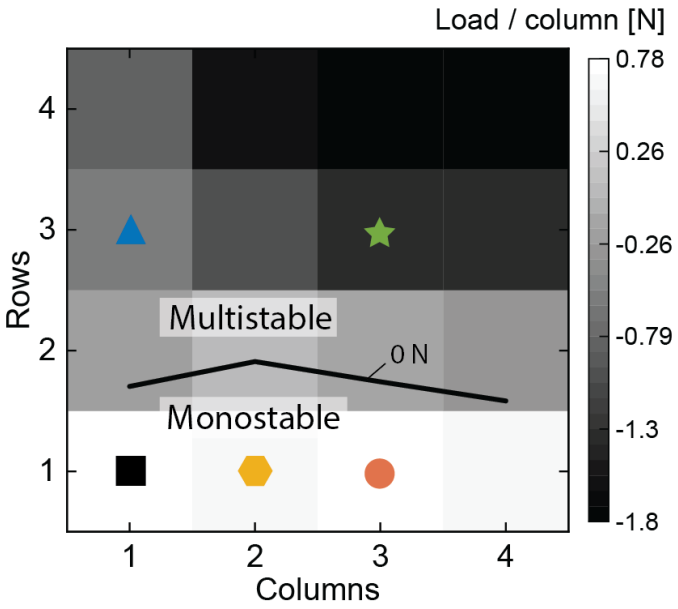


**Fig. S8.** Phase diagram extracted from uniaxial tensile tests (including the ones shown in Figs. S4 and S5). The diagram shows a distinct monostable region for structures with one row and a distinct multistable behavior for structures with three or more rows. It is further seen that an increasing number of columns is beneficial for multistability, as measured by the relative load (per column) of the lowest valley value (bi-/multistable if negative).

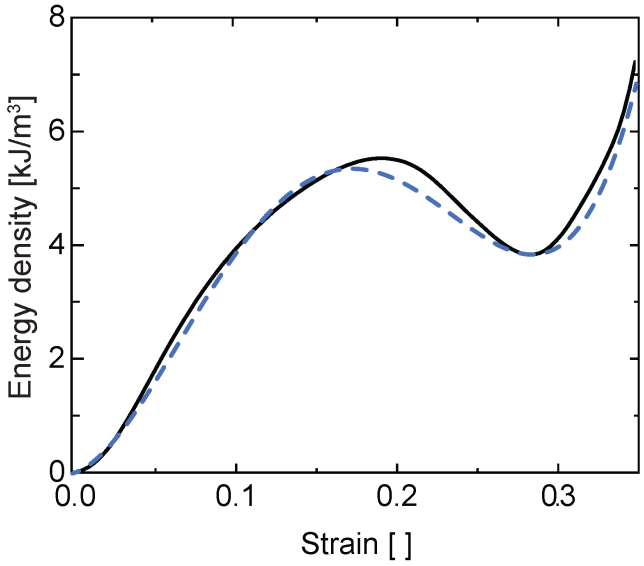


**Fig. S9.** Strain energy density $\psi$ vs. volumetric expansion strain, as extracted from FEA (solid line) and as used in the continuum model (dashed line). The latter is a best-fit quartic polynomial of the former. This potential is used for simulations in Fig. 3. The other potentials used in Figs. 4 and 5 are analogous (see the polynomial coefficients in Table 1).

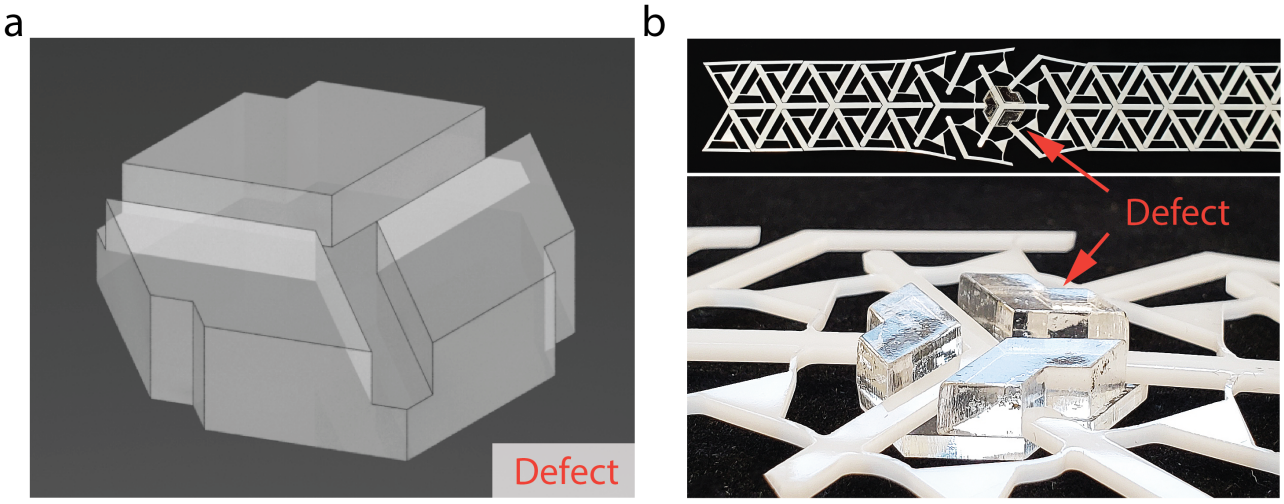


**Fig. S10.** Zoom-in of the defect that prevents unit cells from collapsing. a) cartoon rendering. b) photograph showing the transparent defect with the area around the defect being expanded.

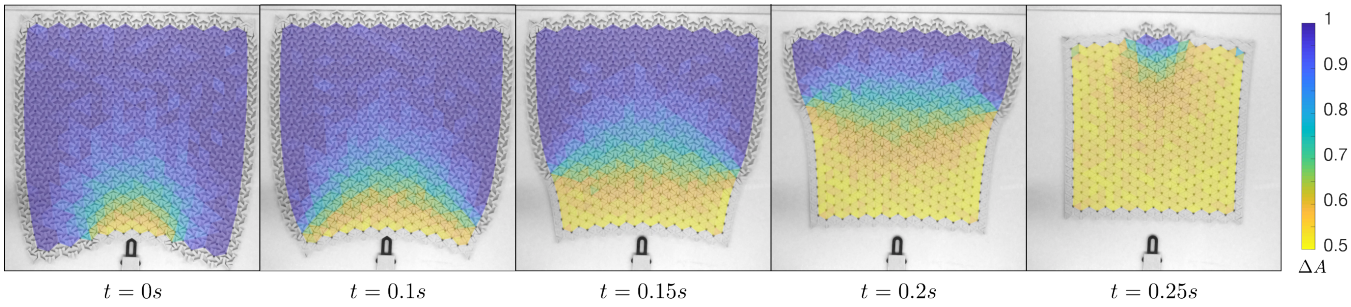


**Fig. S11.** Snapshots of propagation of transition wave in a larger 2D sample showing a curved front (see Movie S5).

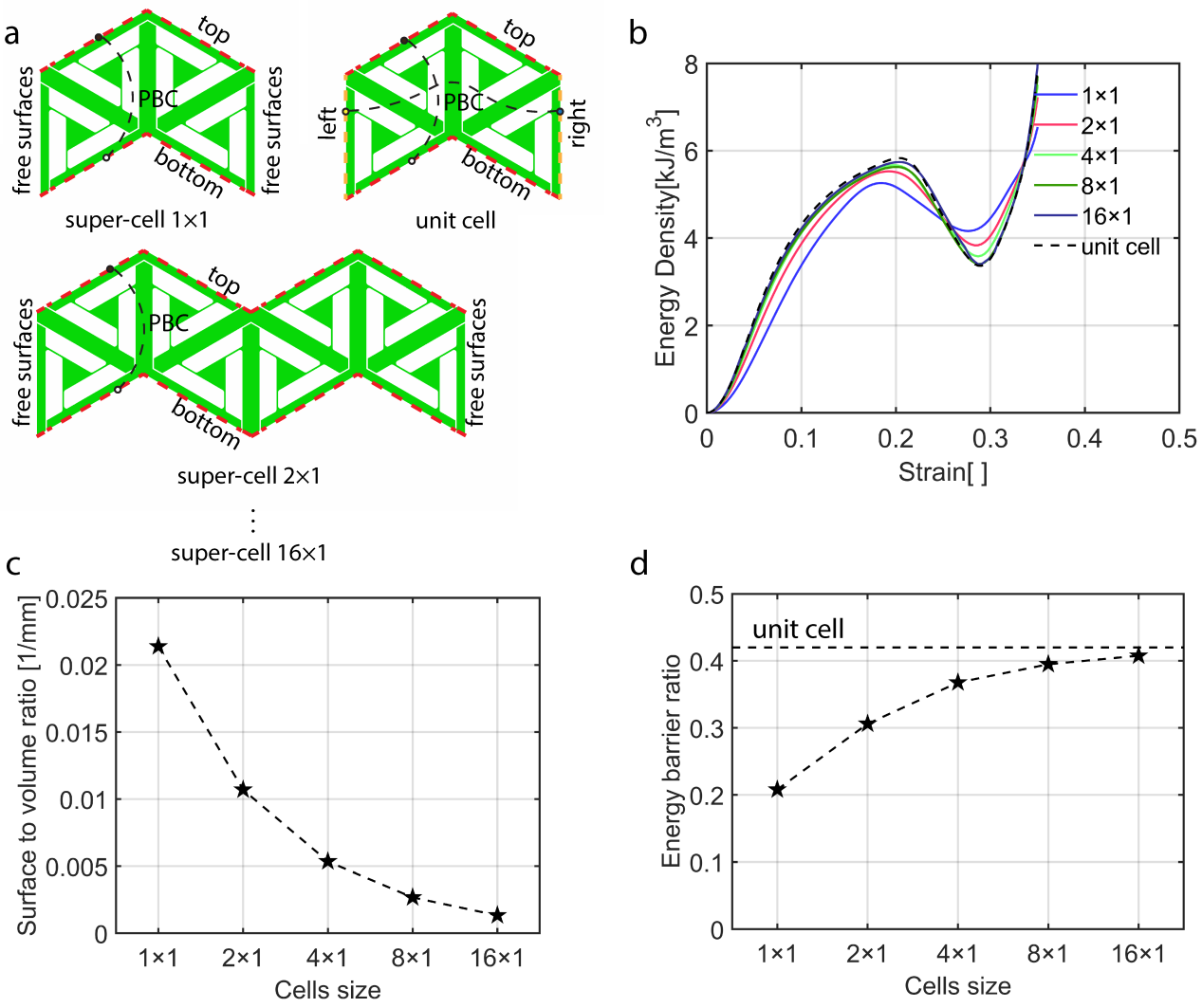


**Fig. S12.** Illustration of free surface effects. (a) To better illustrate the effect of free surfaces, we simulated the response of a $1\times1$ unit cell with periodic boundary conditions (PBCs) applied on all edges and super-cells comprising $1\times1$, $4\times1$, $8\times1$ and $16\times1$ units with PBCs applied only at their bottom and top edges. For such super-cells the vertical edges are free, so that these results allow us to investigate the surface effects. (b) Evolution of the strain energy density as a function of strain for all considered cells. (c) Surface-to-volume ratio for all considered cells. (d) Ratio of well energy to energy barrier for all considered cells. We find that, if the super-cell is sufficiently small (i.e., if the ratio of surface to volume is sufficiently large), the free surfaces affect the strain energy as well as the energy barrier ratio. Conversely, the effect of free surfaces loses importance as the number of units in the super-cell increases, and for sufficiently large super-cells the strain energy converges to that of the periodic unit cell. These results demonstrate that for structures of limited size the strain energy density function used in the continuum model is to be adjusted to account for the effect of free surfaces (as opposed to modeling the bulk response). For structures with rectangular geometry we can directly use these results to identify the strain energy to be used in the continuum model (while for more complex shapes with free surfaces further calibration of the parameters may be required).

**Movie S1. Guiding transition front**

Experimental demonstration of guided transition waves in a 2D periodic multistable network. Loaded by a point force on the left, a transition front propagates through the structure, transforming unit cells from an open (strained) to a closed (unstrained) state as the domain wall passes by. Lattice defects and boundaries can be used effectively to predicatively guide the wave in the laser-cut polymer sheet (the right boundary acts as a rigid wall here).

**Movie S2. 1D transition wave**

Experimental realization of a 1D transition wave in a long multistable chain compared with numerical result from the continuum model. Upon initiation from the left, a 1D transition wave travels through the structure.

**Movie S3. 2D transition wave**

Experimental observations of transition waves propagating through 2D structures (after initialization in the fully open configuration, each transition wave is triggered by a point load applied by the black indenter). Waves are controlled by boundary conditions (e.g., boundary application sites) as well as by defects (e.g., point defects realized by non-transforming open unit cells). Examples show free transition wave propagation in two directions, wave pinning, wave deflection and rotation. Numerical results obtained from the continuum model are in good qualitative agreement with experimental findings, with differences stemming mainly from imperfections and size effects.

**Movie S4. Transition waves in complex structures**

The continuum model is used to explore and expand the design space and realize transition waves in various reconfigurable complex systems,as demonstrated by the following simulated examples:

First, by combining the effects of point defects and free surfaces, a transition front is designed to produce a serpentine motion suitable e.g. locomotion of soft robots.

Second, combining point defects with complex shapes having interior and exterior surfaces adds functionality such as splitting and merging of waves, resulting in morphing devices as demonstrated in a reconfigurable body.

Third, a hollow tube made of a multistable sheet with four different unit cell geometries in five sections (each producing a distinct energy landscape) results in a structure in which the transition wave adjusts its speed in each section. The color map shows the relative change in unit cell area.

**Movie S5. Transition wave in a large 2D sample**

Propagation of transition wave in a large 2D sample showing a curved front.

## References


1. M Senn, C Eberl, Digital image correlation and tracking. *[Computer Software] https://uk. mathworks. com/matlabcentral/fileexchange/50994-digital-image-correlation-andtracking* (2015).
2. N Nadkarni, C Daraio, R Abeyaratne, DM Kochmann, Universal energy transport law for dissipative and diffusive phase transitions. *Phys. Rev. B* **93**, 104109 (2016).
3. J Qiu, JH Lang, AH Slocum, A curved-beam bistable mechanism. *J. microelectromechanical systems* **13**, 137–146 (2004).